High-resolution mapping of infraslow cortical brain activity enabled by graphene microtransistors

Eduard Masvidal-Codina[1], Xavi Illa[2,1], Miguel Dasilva[3], Andrea Bonaccini Calia[4], Tanja Dragojević[5], Ernesto E. Vidal-Rosas[5], Elisabet Prats-Alfonso[2,1], Javier Martínez-Aguilar[1,2], Jose M. De la Cruz Sanchez[4], Philippe Godignon[1], Gemma Rius[1], Alessandra Camassa[3], Elena Del Corro[4], Jessica Bousquet[4], Clement Hébert[4], Turgut Durduran[5,6], Rosa Villa[1,2], Maria V Sanchez-Vives[3,6], Jose A Garrido[4,6]* and Anton Guimerà-Brunet[1,2]*

1 Institut de Microelectrònica de Barcelona, IMB-CNM (CSIC), Esfera UAB, Bellaterra, Spain

2 Centro de Investigación Biomédica en Red en Bioingeniería, Biomateriales y Nanomedicina (CIBER-BBN), Madrid, Spain

3 Institut d'Investigacions Biomèdiques August Pi i Sunyer (IDIBAPS), Barcelona, Spain

4 Catalan Institute of Nanoscience and Nanotechnology (ICN2), CSIC and The Barcelona Institute of Science and Technology (BIST), Campus UAB, Bellaterra, Barcelona, Spain

5 ICFO-Institut de Ciéncies Fotòniques, The Barcelona Institute of Science and Technology, Castelldefels, Barcelona, Spain

6 Institució Catalana de Recerca i Estudis Avançats (ICREA), Barcelona, Spain

* Correspondence:
anton.guimera@imb-cnm.csic.es; joseantonio.garrido@icn2.cat

Keywords: cortical spreading depression, DC-ECoG, graphene, infraslow.

1 Abstract

2 Recording infraslow brain signals (< 0.1 Hz) with microelectrodes is severely hampered by current
3 electrode materials, primarily due to limitations resulting from voltage drift and high electrode
4 impedance. Hence, most recording systems include high-pass filters that solve saturation issues but
5 come in hand with loss of physiological and pathological information. In this work we use for the
6 first time flexible epicortical and intracortical arrays of graphene solution-gated field-effect
7 transistors (gSGFETs) to map cortical spreading depression in rats and demonstrate that gSGFETs
8 are able to record infraslow signals alongside with signals in the typical local field potential
9 bandwidth. This capability results from the direct field-effect coupling of the active transistor, in
10 contrast to standard passive electrodes, as well as from the electrochemical inertness of graphene.
11 Taking advantage of such functionality, we envision broad applications of gSGFET technology for
12 monitoring infraslow brain activity both in research and in the clinic.

13 Recently, there has been a particular resurgence of interest in fluctuations of brain activity occurring
14 at < 0.1 Hz, commonly referred to as very slow, ultraslow or infraslow activity (ISA)[1]. ISA is
15 suggested to have a unique neurophysiological basis[2], and to be indicative of brain states (e.g. sleep,
16 anesthesia, coma, wakefulness)[2-4]. ISA is also correlated with resting-state networks in functional
17 magnetic resonance imaging[5] and may significantly contribute to the high variability observed in the
18 time course of physiological signals[6,7]. Interestingly, spreading depolarizations[8], and more
19 specifically, cortical spreading depression (CSD), occur at infralow frequencies. CSD is defined as a
20 slowly propagating wave of near-complete depolarization of neurons and astrocytes followed by a
21 period of electrical activity suppression. CSD is often triggered in individuals suffering stroke or
22 brain injury as well as migraines and recent research has shown that CSDs play a significant role in
23 brain pathophysiology[9-11]. Therefore, monitoring ISA can be very valuable for clinical diagnosis,
24 prognosis and therapy in neurocritical care[12-14].

25 Non-invasive techniques such as electroencephalography (EEG) and magnetoencephalography
26 (MEG) have been used to study ISA[15,16]. However, their limited spatial resolution, and averaged
27 signal impose serious limitations, e.g. EEG alone is not sufficient for non-invasive CSD
28 detection[13,17]. Hence, invasive electrophysiological techniques are the most widely used to record
29 infraslow brainwaves. The proper recording of ISA requires the use of direct-coupled amplifiers and
30 extremely stable and low-impedance invasive electrodes. Traditionally, liquid-filled glass
31 micropipettes are used, which allow only one or few-point measurements[18]. For higher spatial
32 resolution and mapping, non-polarizable silver/silver chloride (Ag/AgCl) electrodes could be used,
33 which prevent charge accumulation at the interface and therefore voltage drift. However, due to the
34 toxicity of silver, the use of such electrodes for human or chronic animal *in vivo* monitoring is not an
35 option[19]. This has fostered the search for alternative microelectrode materials with low impedance
36 and drift although none has yet been found capable of offering comparable performance as Ag/AgCl
37 electrodes[20]. So, ISA recordings in humans are currently performed with platinum electrodes, which
38 challenge CSD detection due to artifacts and transients[21]. Furthermore, as is discussed in this work,
39 miniaturization of electrode size to achieve higher spatial resolution causes intrinsic high-pass
40 filtering of ISA due to the associated electrode impedance increase[22,23]. Invasive optical techniques
41 such as calcium imaging are also used to monitor ISA, but still nowadays have serious challenges to
42 resolve high-frequency activity for a large number of neurons[24,25] and their intrinsic need of
43 indicators limits the translation to the clinics. Therefore, a technique which allows for measuring
44 large-scale, high-spatiotemporal resolution recordings including infraslow frequencies in a
45 potentially fully implantable, nontoxic, clinical-scale system is still missing (Table S1).

46 Alternatively to the commonly used microelectrode technology, recording electrophysiological
47 signals with field-effect transistors (FET) offers several advantages including that they are less
48 sensitive to environmental noise thanks to their intrinsic voltage-to-current amplification, and that
49 they can be easily multiplexed[26]. Nonetheless, the difficulties to combine high gate capacitance and
50 carrier mobility silicon FETs with flexible materials has historically hampered its use for *in vivo*
51 recordings[27]. Graphene solution-gated field-effect transistors (gSGFETs) have been proposed to
52 potentially overcome all previous drawbacks at once[28]. The two-dimensional nature of graphene
53 provides the highest surface-to-volume ratio possible, making graphene very sensitive to charges at

54 its surface; further, its flexibility allows gSGFETs to be embedded in ultra-soft and flexible
55 substrates without loss of performance[29]. Moreover, the wide electrochemical window and
56 biocompatibility of graphene allows direct contact with biological fluids and tissues and ensures a
57 safe operation in *in vivo* conditions[30]. Taking advantage of the above-mentioned properties, in
58 previous works, we demonstrated that gSGFETs are able to record local field potentials[31,32].

59 In this work we investigate the potential of graphene microtransistors to record infraslow brain
60 activity by performing *in vivo* recordings where we use, for the first time, gSGFETs for both
61 epicortical and intracortical mapping of cortical spreading depression. We found that graphene
62 microtransistors are excellent devices for recording infraslow signals and, furthermore, they do not
63 compromise the acquisition of signals in the conventional local field potential bandwidth. We also
64 demonstrate that gSGFET technology can be used in combination with optical techniques, such as
65 laser speckle contrast imaging, to obtain 2-D maps of the neurovascular coupling.

## 66 Structure, fabrication and characterization of gSGFET arrays

67 A gSGFETS is a device in which graphene is used as channel material, contacted by two metal leads
68 (source and drain terminals), and is immersed in an electrolyte solution where a reference electrode is
69 used as gate terminal (Fig. 1a). We fabricated flexible probes containing arrays of gSGFETs in both
70 epicortical and intracortical designs. In particular, a 4x4 array of 100 µm wide by 50 µm long
71 graphene channels was designed for epicortical recordings while a design consisting of a linear array
72 of 15 graphene channels (80 µm width, 30 µm length) was used for intracortical recordings (Fig. 1b).
73 Both array designs were fabricated on a 10 µm thick polyimide layer coated on a 4-inch silicon wafer
74 using the process previously reported in Hébert et al.[32]. Flexible gSGFET arrays were placed in zero
75 insertion force connectors for interfacing with recording electronics (Fig. 1c). The transfer curve,
76 drain current (I_{ds}) *vs* gate-source voltage (V_{gs}), of all gSGFETs in each array was measured with a
77 fixed drain-source voltage (V_{ds}). The dispersion of the charge neutrality point (CNP=243.6 ± 6.1
78 mV), which is the minimum of the transfer curve, indicates the homogeneity of the transistors (Fig.
79 1d). Importantly, since the V_{gs} and V_{ds} bias are shared, the small CNP dispersion allows near-optimal
80 recording performance for all gSGFETs in the same array. Figure 1e shows the sum of leakage
81 current (I_{gs}) for all gSGFETs in the array, which is in the nA range throughout the voltage sweep,
82 demonstrating the good insulation of the passivation layer and the negligible reactivity of the
83 graphene. Furthermore, we measured the frequency response of the transconductance (g_m) of a
84 gSGFET, which indicates the efficiency of the signal coupling ($\partial I_{ds}/\partial V_{gs}$), obtaining constant values
85 in a wide bandwidth including inflalow frequencies (Fig. 1f-g). The negative g_m for V_{gs} values lower
86 than the CNP results in an inversion (180º phase) of the signals measured at such bias; for V_{gs} values
87 higher than the CNP the signal phase is preserved.
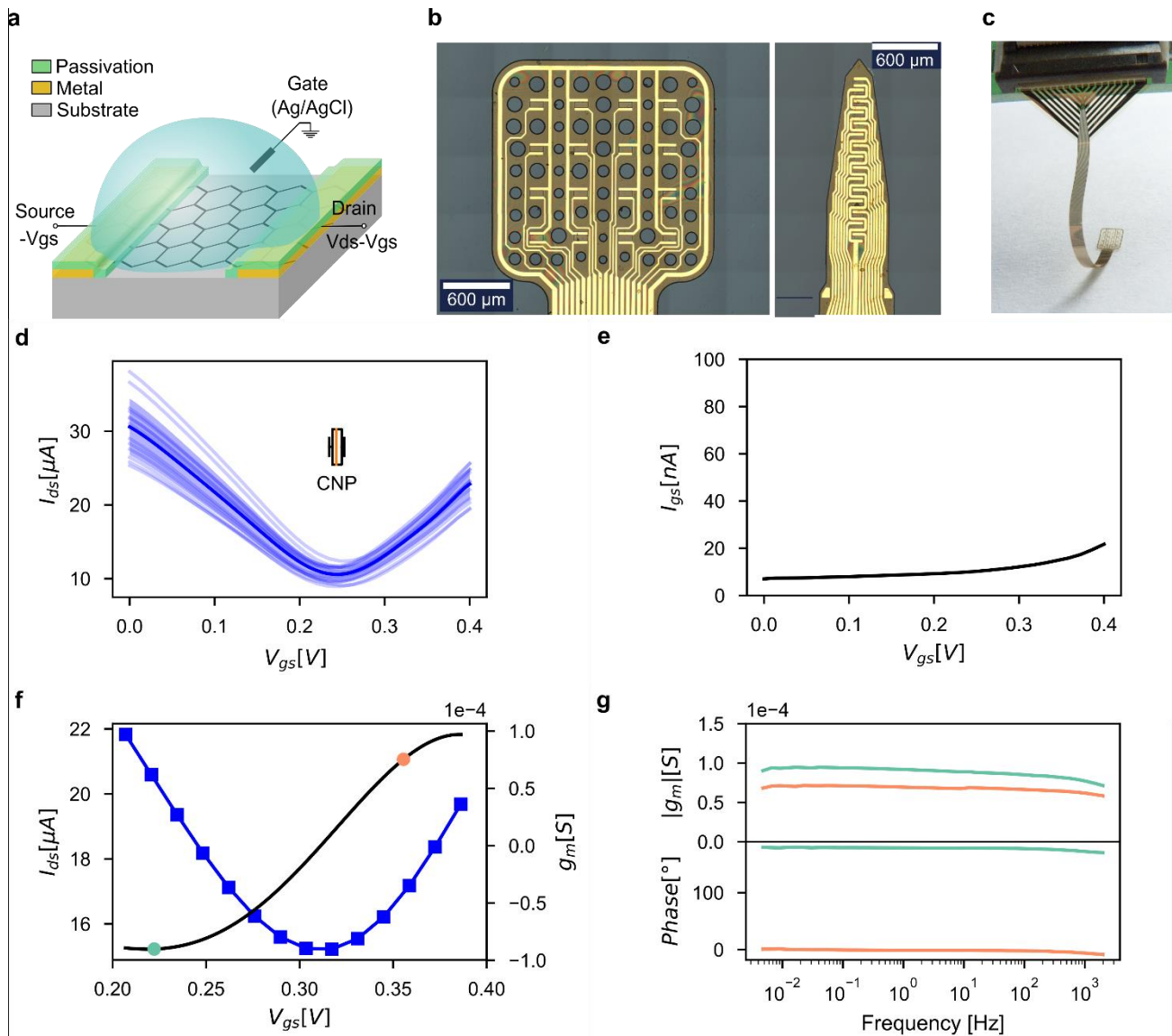
Fig. 1 | Flexible graphene solution-gated field-effect transistor array technology and characterization. a, Schematic of a graphene transistor polarized in common gate mode. **b**, Optical microscope images of the active area of the 4×4 gSGFET array and the 15 channel intracortical array. **c,** Photograph of the neural probe after peeling from the wafer and being introduced into a zero insertion force connector. **d-g,** Steady-state and frequency response characterization of a 100x50-μm^2 gSGFET array in 10 mM phosphate buffered saline (PBS) and with a drain-source voltage bias (V_{ds}) of 50 mV. **d,** gSGFET transfer curves (blue lines), drain-source current (I_{ds}) *vs* gate-source voltage (V_{gs}), together with the mean (dark blue) and standard deviation (blue shade). Boxplot inset shows charge neutrality point dispersion. **e,** Leakage current (I_{gs}) of all gSGFETs in the array. **f,** Transfer curve (blue squares and line) and its first derivative (transconductance (g_m), black line) of a gSGFET. **g,** Frequency response of the transconductance at two different points of the transfer curve (**e**): V_{gs} lower than the CNP (green), where g_m is negative resulting in a signal inversion (180º phase); and V_{gs} higher than the CNP (orange), where g_m is positive and thus results in no inversion (0º phase) . Independently of the branch of the transfer curve where a gSGFET is polarized, the module of g_m is similar to the steady-state value for a wide bandwidth ($\approx$ 0 - 1 kHz).

5
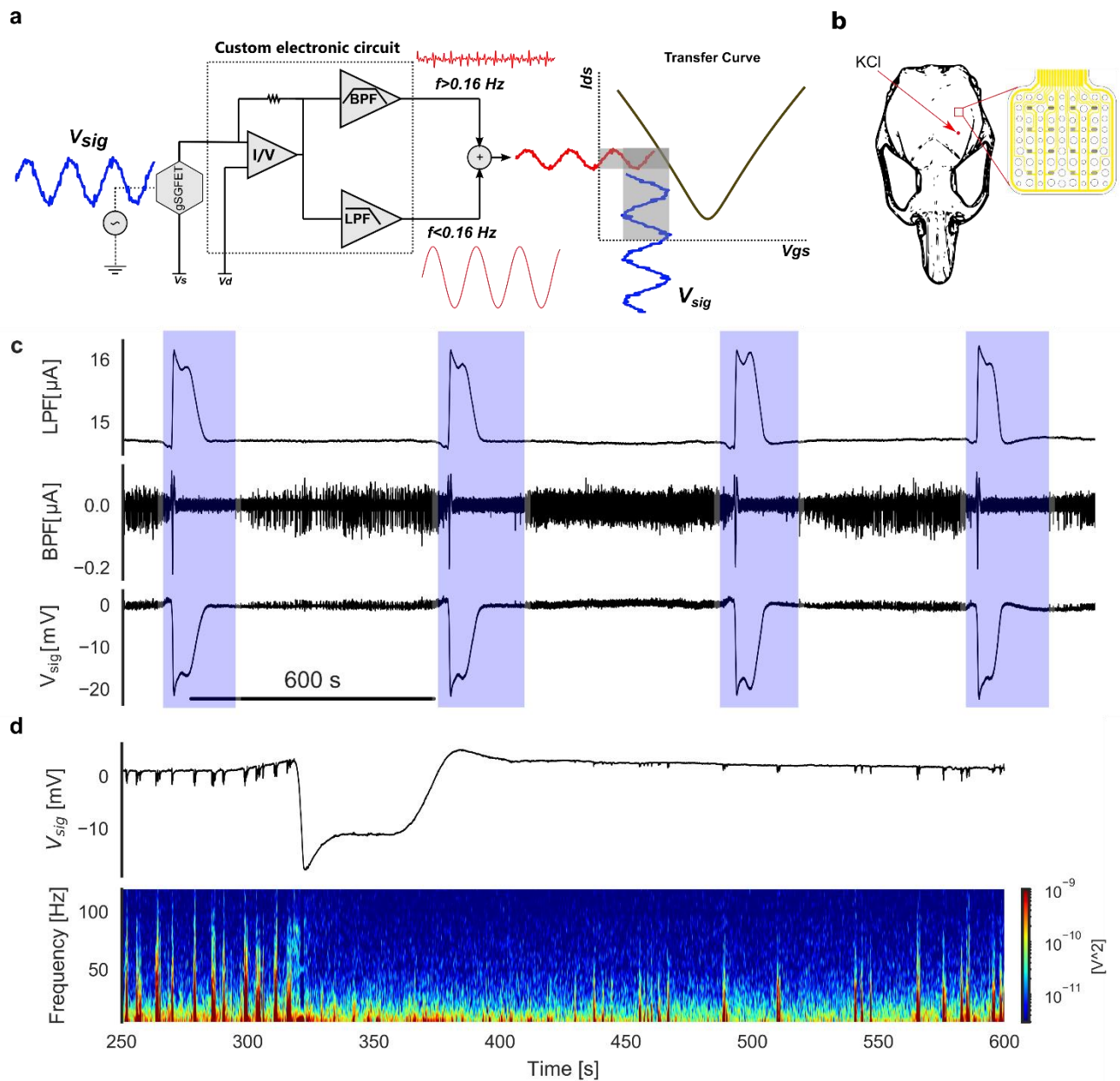
Fig. 2 | Infraslow, local field potential, and wide-band *in vivo* gSGFET recordings of cortical spreading depression (CSD). a, Schematic of the gSGFET recording setup and signal post processing methodology. The custom electronic circuit is used to perform the *in vivo* characterization (transfer curve) and record the transistor current in the low-pass-filtered (LPF) band and the band-pass-filtered (BPF) band. From the combination of both signals and taking into account the current-to-voltage conversion, the wide-band signal (V_{sig}) is obtained. **b,** Schematic of the location of the gSGFET array and the frontal craniotomy where 5mM KCl was applied to induce CSDs. **c,** Electrophysiological recordings obtained with a gSGFET epicortical array during the induction of four CSD events (blue shade). From top to bottom: current LPF signal, current BPF and voltage-converted wide-band signal. **d, V**oltage-converted wide-band signal of a CSD event and spectrogram showing the silencing of activity.

In vivo wide-band recordings

Cortical spreading depression[9,11,18] was chosen to illustrate the capabilities of graphene transistors to record in a wide bandwidth. Experimentally, two craniotomies were performed over the left hemisphere of isoflurane-anaesthetized Wistar rats: a larger craniotomy over the primary somatosensory cortex, where the epicortical probe was placed, and a smaller one in the frontal cortex, where 5 mM KCl was applied locally to induce CSD (Fig. 2b). A custom electronic circuit allowed us to simultaneously record at two frequency bands: low-pass filtered band (LPF, ≈0-0.16 Hz) and band-pass filtered band (BPF, 0.16 Hz-10 kHz) with different gains (10^4, and 10^6 respectively) to avoid amplifier saturation due to the high-amplitude CSD signal. In a first set of experiments, we recorded the LPF and BPF current signals with an epicortical gSGFET array during the induction of CSD events (Fig. 2c). The graphene transistors were polarized in the hole conduction regime, i.e. V_{gs} < CNP (negative g_m); therefore, the recorded LPF and BPF current signals are inverted with respect to the voltage signal occurring at the gate. The LPF signal shows the very slow CSD event whereas the BPF signal corresponds to the local field potential, revealing the silencing of activity typical of cortical spreading depression. After summation of the LPF and BPF signals and then transforming the current into a voltage signal (using the transistor transfer curve I_{ds} - V_{gs} recorded *in vivo* prior to the start of the recordings), the wide-band electrophysiological signal can be obtained (see Fig. 2 a, c). In each CSD event a small positive shift of 1-2 mV generally precedes the depression, immediately after which a steep negative change (≈ -20 mV) can be observed, which slowly recovers during the next minute or so. The CSD-associated silencing of high-frequency activity and its progressive recovery is shown in the voltage wave and spectrogram of Fig. 2d.

SGFETs *vs* microelectrodes: comparison of ISA recording capabilities

A second set of experiments was designed to compare the performance of gSGFETs with microelectrodes in *in-vivo* direct-coupled recordings. CSD was induced and simultaneously recorded with an gSGFET epicortical array located more posterior to a neural probe containing groups of triodes of 50 µm diameter gold microelectrodes in which one microelectrode of each triode was modified by deposition of platinum black to lower its impedance (Fig. S2). Fig. 3a shows that gold and platinum black recordings exhibit very large and diverse baseline offsets as well as oscillations and drifts (-7.9 ± 3.3 and -3.6 ± 1.6 mV/h), while the gSGFET signals are very stable (1.1 ± 1.0 mV/h). Importantly, gSGFETs record significantly higher amplitude for the CSD events (-13.3 ± 1.8 mV) in comparison with gold (-4.7 ± 1.6 mV) and platinum black (-3.0 ± 0.7 mV) microelectrodes. Figure 3b highlights these two intrinsic limitations of microelectrode technology for the measurement of ISA: polarization-induced drift and signal filtering[20,23].
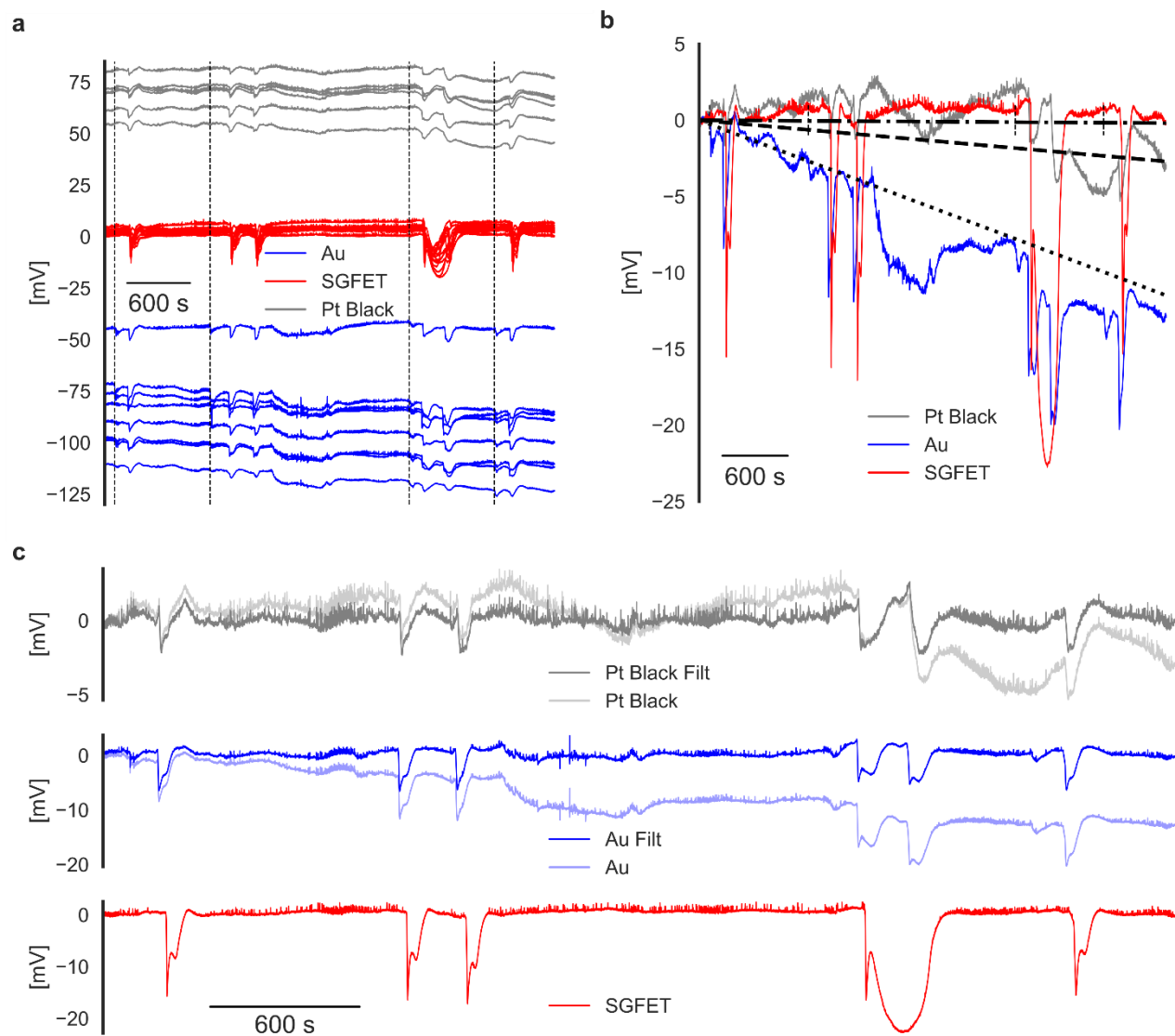
Fig. 3 | Comparison of gSGFET and microelectrode recordings of cortical spreading depressions. a, Direct-coupled recordings of 100x50 µm² gSGFET transistors and gold and platinum black 50 µm diameter microelectrodes. The vertical dashed lines show the time when KCl (5 mM) was applied to induce a CSD. **b,** DC-offset removed recordings of a representative channel of each type. Black lines illustrate the mean drift: dotted and dashed correspond to gold and platinum black microelectrodes, respectively, and the dash-dotted line corresponds to gSGFETs. **c,** DC-offset removed recordings of a representative channel of each class and the same signal filtered at 0.002 Hz to remove oscillations and drift; the gSGFET signal does not require any filtering.

The drift of the baseline potential superimposed over the huge voltage offsets is problematic as it can lead to saturation of the amplifiers used to record the signal. For this reason most microelectrode recording instrumentation include a high-pass filter. More importantly, baseline drift in the form of baseline oscillations in the infralow frequencies, hamper the determination of CSD characteristics such as amplitude or waveform as any high-pass filter used to remove such effects will alter the signal shape (see Fig.3c and Fig. S3). Another intrinsic limitation of microelectrode technology is based on the relation between the microelectrode impedance and the input impedance of the

8

167 recording equipment (Z_e' and Z_a', respectively). The recorded signal (V_{in}) is determined by the
168 voltage divider formed by both impedances:

$$V_{in}(f) = I(f)Z_a'(f) = \frac{V_{sig}(f)\, Z_a'(f)}{Z_a'(f) + Z_e'(f)} \tag{1}$$

169 Eq. (1) implies that when Z_a', is not substantially larger than Z_e', the recorded signals will be
170 attenuated and delayed with respect to V_{sig} [22]. By measuring the impedance of both electrode types
171 and modelling the preamplifier impedance with the values reported by the manufacturer, we obtained
172 the voltage gain (V_{in}/V_{sig}) of the equivalent circuit formed by the recording electrode and the
173 amplifier, see Fig. 4a-b. For 50 µm diameter gold microelectrodes, an attenuation lower than 50% is
174 expected which is in agreement with the experimental results. For platinum black we attribute the
175 higher attenuation than predicted to electrochemical processes that impact the electrode response at
176 very low frequencies. It is important to highlight that the $Z_a' \gg Z_e'$ requirement to achieve a voltage
177 gain equal to 1 is compromised when the electrode area is scaled down, due to the inverse relation
178 between electrode impedance and its area leading to high-pass filtering of the recorded signals.

179 In contrast, the results of the *in vivo* comparison provide evidence that gSGFETs are able to record
180 signals in a wide bandwidth, which we assign to the following main reasons. First, graphene exhibits
181 an excellent DC stability, as demonstrated by low *in vivo* drift. We attribute this to the low density of
182 states of pristine graphene near the Fermi level, which decreases the overall electronic overlap with
183 redox species[33], and to the low density of extrinsic electron transfer sites, i.e. defects and edges, all
184 contributing to the excellent electrochemical inertness of CVD graphene[24,34,35]. The low leakage
185 current measured (Fig. 1e) also supports the electrochemical inertness. The second reason for which
186 graphene microtransistors can record infraslow signals is related to its working mechanism, which is
187 significantly different from that of electrodes. In gSGFETs, voltage oscillations near the active
188 graphene channel modulate the current flow along it (see schematic and small-signal model in Fig.
189 4a). Eq. 2 shows the relation between the recorded current (I_{ds-rec}) and the signal (V_{sig}):

$$I_{ds-rec}(V_{gs}, V_{sig}) = I_{ds}(V_{gs}) + i_{ds}(V_{gs}, V_{sig}) = I_{ds}(V_{gs}) + g_m(V_{gs} + V_{sig})\, V_{sig} \tag{2}$$

190 where I_{ds} is the current at the bias point V_{gs} and i_{ds} the current variation induced by the gate signal.
191 This equation is valid and frequency-independent as long as g_m is also frequency-independent. We
192 had previously reported that gSGFETs exhibit a transconductance that is independent of frequency
193 over the local field potential bandwidth[32]. In this work (Fig. 1g), we have confirmed that the
194 transconductance of gSGFETs remains constant down to infralow frequencies. Importantly, scaling
195 down the size of a transistor does not result in a decrease of g_m at infralow frequencies.

196
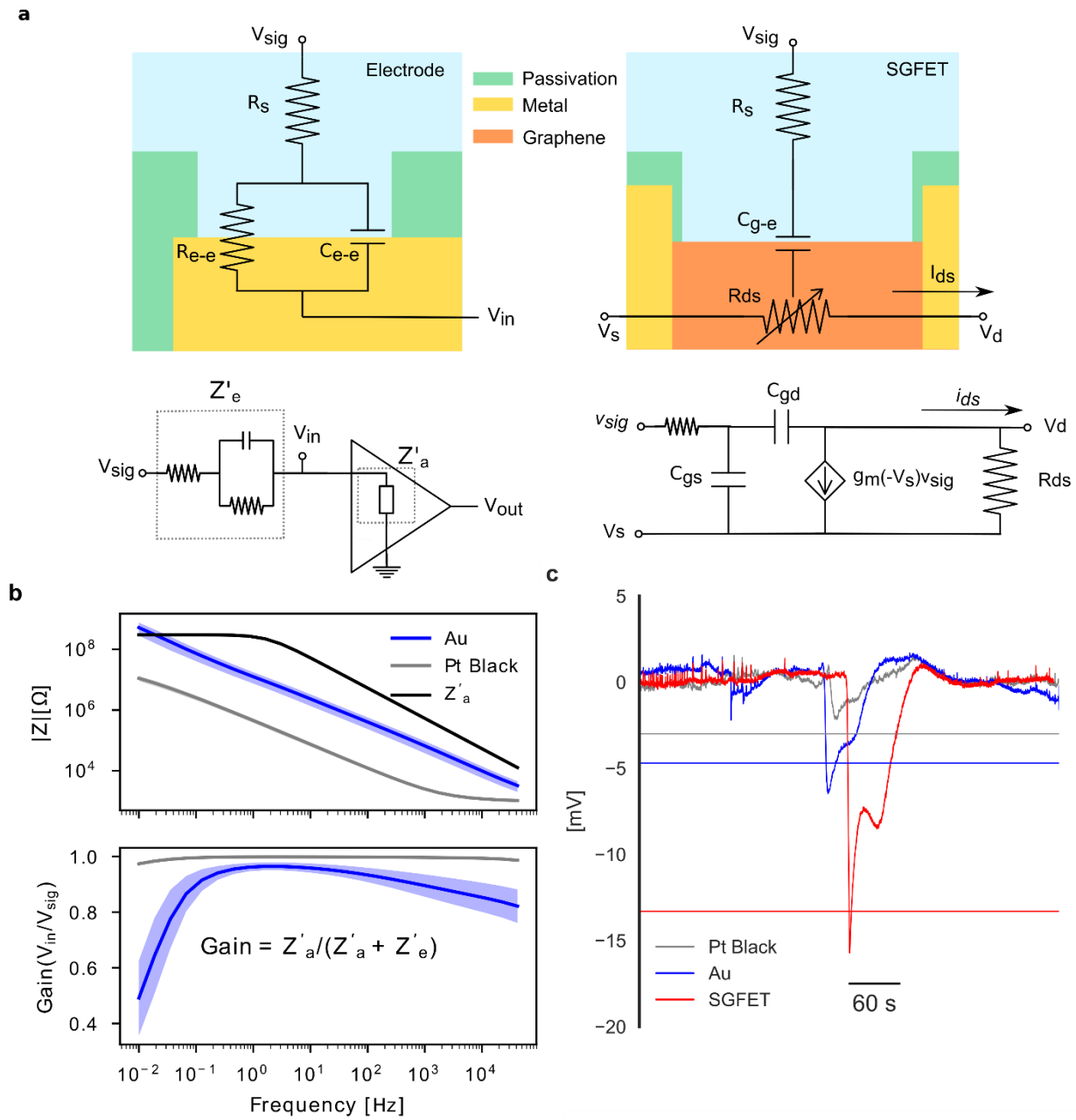
Fig. 4 | Microelectrode and gSGFET recording modes and signal filtering. a, Cross-sectional view and superimposed electric equivalent circuit models of a recording electrode and a gSGFET. For an electrode, the electrode-electrolyte interface, is modelled simply as a capacitor and a resistor in parallel (R_{e-e}, C_{e-e}). The voltage divider formed by Z'_e and Z'_a, the effective electrode and amplifier impedance, respectively, determines V_{in}, the voltage at the input of the amplifier. R_s represents the electrolyte resistance. In the case of a gSGFET, V_{sig} modulates the graphene channel resistance (R_{ds}) by field-effect through the gate capacitance (C_{g-e}), which results in current variations (i_{ds}) proportional to the transconductance value at the bias point, plus the voltage signal (which is mostly negligible for small amplitude electrophysiological signals), as seen in the small signal model. **b,** Mean and standard deviation of the impedance module (experimental data) of the 50 μm diameter gold (blue) and platinum black (grey) microelectrodes together with the amplifier impedance (Z'_a) and calculated voltage gain (V_{in}/V_{sig}) for each microelectrode type. **c,** Recordings of a CSD event for each type of microelectrodes and a gSGFET. Horizontal lines represent the mean value of CSD amplitude.

10

Mapping CSD with gSGFETs

As an example of the potential of gSGFET technology we mapped the propagation of CSD events using a 4x4 epicortical gSGFET array and compare the signals with what is observed in conventional high-pass filtered recordings (Fig. 5a-b). The recording of the whole CSD event with the gSGFET array reveals that while the onset of the negative shift is similar for all gSGFETs, there is much more variety in the subsequent recovery, with some transistors exhibiting a second negative shift with higher amplitude than the first one. This effect can also be observed in the last frames (corresponding to 80 s and 90 s) of the spatial maps of gSGFET recordings (Fig. 5b) where recovered and still depressed brain areas coexist. Importantly, this information is lost in conventional microelectrode recordings, where only the CSD onset is observed due to the high pass filter in the recording electronics. The following results are referred to a sample of 10 CSDs collected from two different subjects in the somatosensory cortex: we found that the mean duration of CSD events is 47.24 ± 7.65 s and a speed of propagation of 7.68 ± 1.35 mm/min, in agreement with the literature defining CSDs as infraslow brainwaves. Further details of the propagation analysis and results (Fig. S7 can be found in the Supplementary Information.

It is known that under physiological conditions there is a normal neurovascular response defined by vasodilatation and increased rCBF due to spreading depolarization that causes spreading hyperemia[9]. However, most studies on CSD neurovascular coupling have been performed with mapping techniques for the rCBF while electrical activity is measured only at two sites with glass micropippetes[5]. Here, taking advantage of the gSGFET technology, we designed an experiment in which we could simultaneously map both variables. Fig. 5c provides further evidence of the spreading depolarization and hyperemia neurovascular coupling. We used a non-contact, wide-field technique, laser speckle contrast imaging (LSCI)[36], which consists in the measurement of the fluctuations of the laser speckle pattern produced by coherent light when it is scattered from an illuminated object. *In vivo*, the presence of dynamic scatterers, mainly moving red blood cells, allows to image variations of rCBF[37]. Experimentally, a craniotomy was performed in a Wistar rat and a continuous-wave temperature controlled laser diode and a camera were mounted to image a wide area inside which an epicortical 16-channel gSGFET array was placed. After 5mM KCl administration, CSD was induced, which was followed by an increase in rCBF that slowly returned (4-5minutes) to basal values. Importantly, gSGFETs did not hamper rCBF measurements, as metal microelectrodes do, and thus allow the measurement of rCBF and electrophysiological signals simultaneously over the same area.

To further illustrate the potential of gSGFET technology and taking advantage of the design versatility offered by this technology, we performed *in vivo* experiments with intracortical probes consisting of a linear array of 15 gSGFETs spanning the entire depth of the cortex (Fig. 6a). From either the ordered recording or the spatiotemporal voltage map (Fig. 6b), it can be seen how CSD occurs in the whole cortex depth. These results highlight the capability of gSGFET technology to reveal the rich pattern of infraslow signals in the cortex; in this particular case, a transition from a superficial long depolarization to a shorter one preceded and followed by a hyperpolarization in the deeper layers is clearly observed. The origin of such depth-dependent effect is not well understood

249 and will be the target of further investigations, taking advantage of the demonstrated capability of
250 gSGFET technology to monitor ISA with high spatial resolution.

251

252
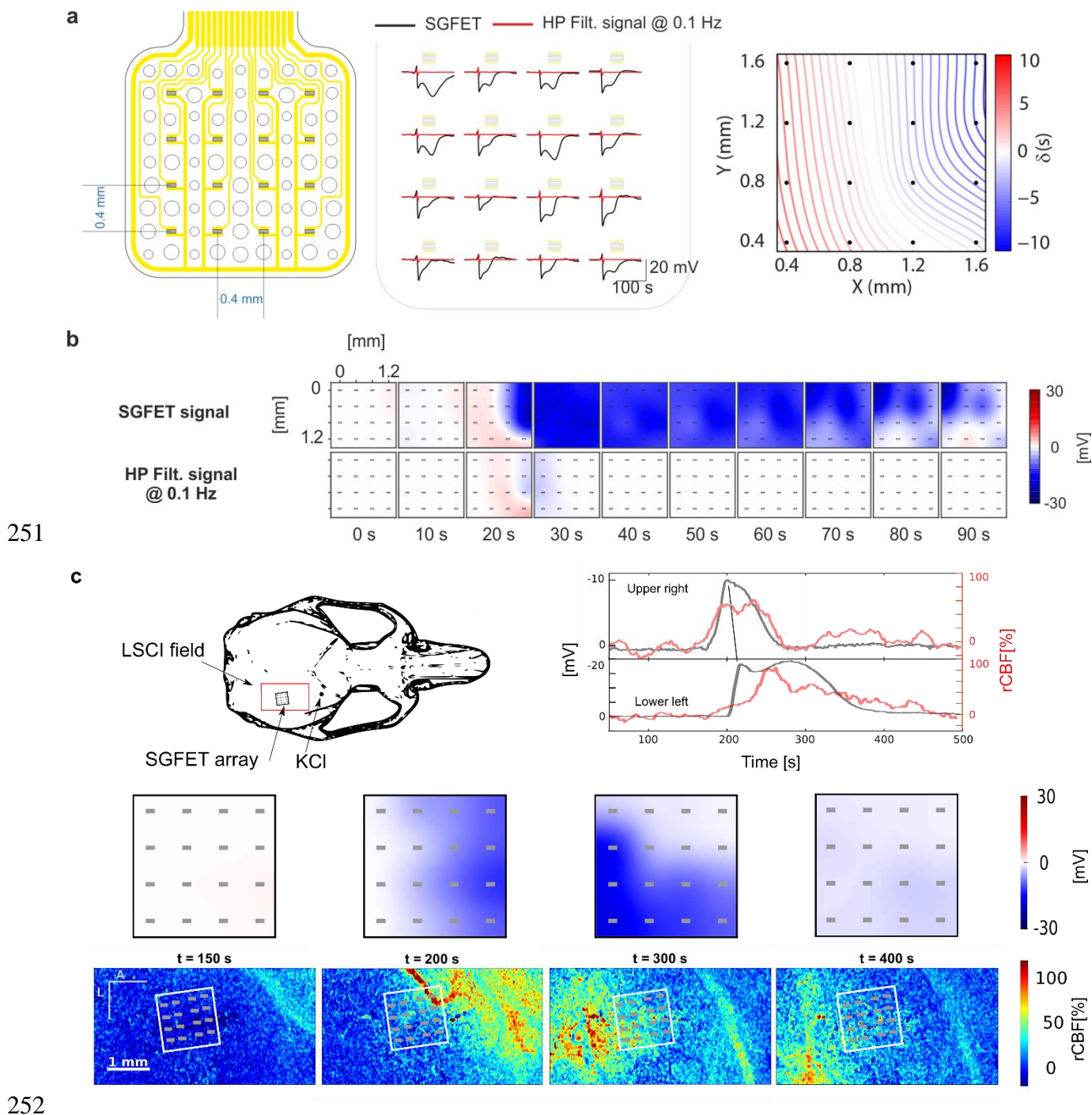
253 **Fig. 5 | Graphene transistor arrays enable mapping of cortical spreading depression *in vivo*. a,** Infralow
254 frequency signals recorded by a 4x4, 400 µm grid spacing, gSGFET array (black lines) during the occurrence
255 of a CSD event and contour plot of the spatiotemporal course of the CSD. **b,** Interpolated spatial voltage maps
256 showing the propagation of the same CSD event as measured by the 4x4 epicortical gSGFET array. **a,b** High
257 pass filtered recordings at 0.1Hz (red lines in **a** and bottom spatial voltage maps in **b** are included to illustrate
258 the loss of signal information in conventional microelectrode recordings. **c,** Schematic of a rat skull depicting
259 the laser speckle contrast imaging field-of-view and the position of the gSGFET array. Time evolution of the
260 upper right and lower left graphene microtransistors as well as the regional cerebral blood flow at the same

position. Color maps represents the extracellular voltage as measured by the gSGFET array (top) and the relative cerebral blood flow (bottom) at a given time after the induction of a CSD by 5mM KCl.
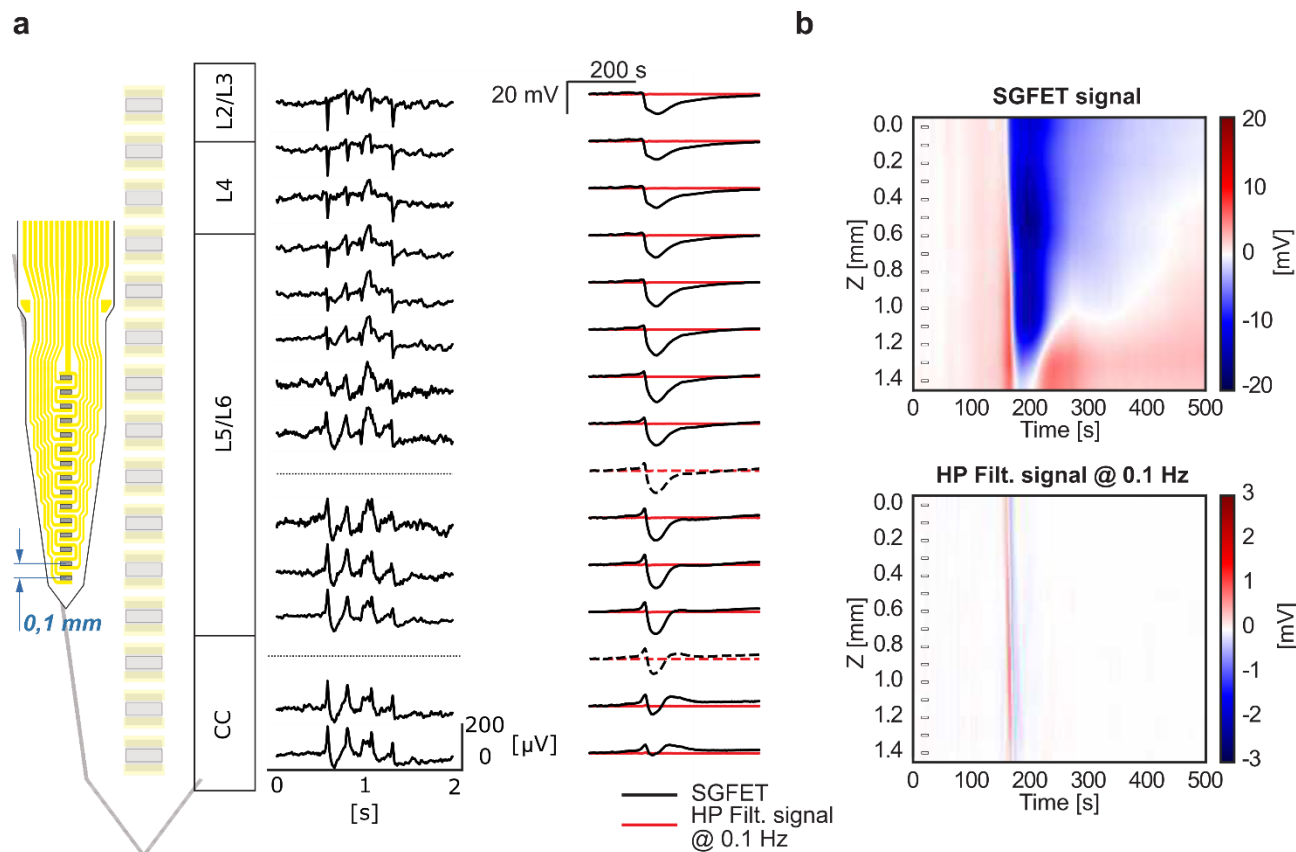
Fig. 6 | Depth profile of infralow-frequency voltage variations induced by cortical spreading depression. a, Layout of the fabricated 15-channel graphene intracortical probe and ordered local field potential recordings. **b,** Low-frequency recordings (black lines) during the occurrence of a CSD event. Dashed lines correspond to broken transistors and illustrate the interpolated signal at that position. Same signal high-pass filtered at 0.1 Hz (red lines) and their spatio-temporal color map are included to illustrate the loss of information in conventional microelectrode recordings.

Outlook

In this work we show that gSGFETs can record neural signals in a wide electrophysiological bandwidth, including infralow (<0.1 Hz) frequencies. There are two main reasons that explain this unique capability: the direct DC-coupling, in contrast to standard passive electrodes, and the excellent electrochemical stability. Making use of such capabilities, gSGFET technology opens the possibility to map infraslow oscillations with high spatiotemporal resolution (epicortically and intracortically) which can lead to a better understanding of the brain regions where ISA is initiated, its propagation to other areas and clarify the interplay of different cellular types, which are yet poorly understood[1,2,38]. The physiological implications of ISA to a wide range of brain functions as also its pathophysiological consequences and contribution to neural disorders would benefit chronic use of gSGFET technology potentially leading to the discovery of new therapies. Additionally, gSGFETs can help in determining ISA relation with higher frequency signals[16,39] and contribute to a better understanding of the genesis of local field potentials[40] and of cortical wave propagation features[41,42].

13

Also, obtained data demonstrate that gSGFETs and LSCI can be used together to map electrophysiological signals and rCBF therefore allowing improved characterization of the neurovascular coupling of ISA. In the particular case of CSDs, gSGFET technology emerges as a potential clinically relevant tool to help determine the relation of CSDs to neural disorders such as migraine, malignant stroke, subarachnoid and intracranial haemorrhage, and traumatic brain injury. If the challenges of translating gSGFET technology to the clinics are surpassed, a first direct application could be for CSD intraoperative monitoring since there is evidence that CSD can occur during neurosurgical procedures[43]. In summary, our work strongly suggests that gSGFET arrays are ideal candidates to fill the gap of a large-scale, high-spatiotemporal recording technology that covers a wide electrophysiological bandwidth in a potentially fully implantable, nontoxic, clinical-scale device. We believe that the demonstrated capabilities of graphene microtransistors constitute a considerable advance in electrophysiological recording technology which could lead to breakthroughs in brain function understanding as well as in clinic diagnosis and treatment.

References

1   Hughes, S. W., Lőrincz, M. L., Parri, H. R. & Crunelli, V. in *Progress in Brain Research* Vol. 193 (eds Eus J. W. Van Someren *et al.*) 145-162 (Elsevier, 2011).

2   Mitra, A. *et al.* Spontaneous Infra-slow Brain Activity Has Unique Spatiotemporal Dynamics and Laminar Structure. *Neuron*, doi:https://doi.org/10.1016/j.neuron.2018.03.015.

3   Lecci, S. *et al.* Coordinated infraslow neural and cardiac oscillations mark fragility and offline periods in mammalian sleep. *Science Advances* **3**, e1602026 (2017).

4   Mitra, A., Snyder, A. Z., Tagliazucchi, E., Laufs, H. & Raichle, M. E. Propagated infra-slow intrinsic brain activity reorganizes across wake and slow wave sleep. *Elife* **4** (2015).

5   Hiltunen, T. *et al.* Infra-slow EEG fluctuations are correlated with resting-state network dynamics in fMRI. *Journal of Neuroscience* **34**, 356-362 (2014).

6   Leopold, D. A., Murayama, Y. & Logothetis, N. K. Very slow activity fluctuations in monkey visual cortex: implications for functional brain imaging. *Cerebral cortex* **13**, 422-433 (2003).

7   Kelly, A. C., Uddin, L. Q., Biswal, B. B., Castellanos, F. X. & Milham, M. P. Competition between functional brain networks mediates behavioral variability. *Neuroimage* **39**, 527-537 (2008).

8   Chung, D. Y. & Ayata, C. in *Primer on Cerebrovascular Diseases (Second Edition)* (eds José Biller *et al.*) 149-153 (Academic Press, 2017).

9   Dreier, J. P. The role of spreading depression, spreading depolarization and spreading ischemia in neurological disease. *Nat Med* **17**, 439-447 (2011).

10   Dreier, Jens P. & Reiffurth, C. The Stroke-Migraine Depolarization Continuum. *Neuron* **86**, 902-922, doi:https://doi.org/10.1016/j.neuron.2015.04.004 (2015).

11   Lauritzen, M. *et al.* Clinical relevance of cortical spreading depression in neurological disorders: migraine, malignant stroke, subarachnoid and intracranial hemorrhage, and traumatic brain injury. *Journal of Cerebral Blood Flow & Metabolism* **31**, 17-35 (2011).

321 12   Hartings, J. A. *et al.* Direct current electrocorticography for clinical neuromonitoring of
322   spreading depolarizations. *Journal of Cerebral Blood Flow & Metabolism*,
323   0271678X16653135 (2016).

324 13   Dreier, J. P. *et al.* Recording, analysis, and interpretation of spreading depolarizations in
325   neurointensive care: review and recommendations of the COSBID research group. *Journal of*
326   *Cerebral Blood Flow & Metabolism*, 0271678X16654496 (2016).

327 14   Kovac, S., Speckmann, E.-J. & Gorji, A. Uncensored EEG: The role of DC potentials in
328   neurobiology of the brain. *Progress in Neurobiology*,
329   doi:https://doi.org/10.1016/j.pneurobio.2018.02.001 (2018).

330 15   Vanhatalo, S., Voipio, J. & Kaila, K. Full-band EEG (FbEEG): an emerging standard in
331   electroencephalography. *Clinical Neurophysiology* **116**, 1-8,
332   doi:http://dx.doi.org/10.1016/j.clinph.2004.09.015 (2005).

333 16   Vanhatalo, S. *et al.* Infraslow oscillations modulate excitability and interictal epileptic activity
334   in the human cortex during sleep. *Proceedings of the National Academy of Sciences of the*
335   *United States of America* **101**, 5053-5057 (2004).

336 17   Hofmeijer, J. *et al.* Detecting Cortical Spreading Depolarization with Full Band Scalp
337   Electroencephalography: An Illusion? *Frontiers in Neurology* **9**,
338   doi:10.3389/fneur.2018.00017 (2018).

339 18   Ayata, C. & Lauritzen, M. Spreading depression, spreading depolarizations, and the cerebral
340   vasculature. *Physiological reviews* **95**, 953-993 (2015).

341 19   Stensaas, S. S. & Stensaas, L. J. Histopathological evaluation of materials implanted in the
342   cerebral cortex. *Acta Neuropathologica* **41**, 145-155, doi:10.1007/bf00689766 (1978).

343 20   Li, C. *et al.* Evaluation of microelectrode materials for direct-current electrocorticography.
344   *Journal of neural engineering* **13**, 016008 (2015).

345 21   Hartings, J. A. *et al.* Direct current electrocorticography for clinical neuromonitoring of
346   spreading depolarizations. *Journal of Cerebral Blood Flow & Metabolism* **37**, 1857-1870
347   (2017).

348 22   Nelson, M. J., Pouget, P., Nilsen, E. A., Patten, C. D. & Schall, J. D. Review of signal
349   distortion through metal microelectrode recording circuits and filters. *Journal of neuroscience*
350   *methods* **169**, 141-157 (2008).

351 23   Stacey, W. C. *et al.* Potential for unreliable interpretation of EEG recorded with
352   microelectrodes. *Epilepsia* **54**, 1391-1401 (2013).

353 24   Kuzum, D. *et al.* Transparent and flexible low noise graphene electrodes for simultaneous
354   electrophysiology and neuroimaging. *Nature communications* **5**, 5259 (2014).

355 25   Deneux, T. *et al.* Accurate spike estimation from noisy calcium signals for ultrafast three-
356   dimensional imaging of large neuronal populations in vivo. *Nature Communications* **7**,
357   12190, doi:10.1038/ncomms12190
358   https://www.nature.com/articles/ncomms12190#supplementary-information (2016).

359 26   Fang, H. *et al.* Capacitively coupled arrays of multiplexed flexible silicon transistors for long-
360   term cardiac electrophysiology. *Nature biomedical engineering* **1**, 0038 (2017).

361 27 Heremans, P. *et al.* Mechanical and electronic properties of thin-film transistors on plastic, and their integration in flexible electronic applications. *Advanced Materials* **28**, 4266-4282 (2016).

364 28 Hess, L. H., Seifert, M. & Garrido, J. A. Graphene transistors for bioelectronics. *Proceedings of the IEEE* **101**, 1780-1792 (2013).

366 29 Kim, B. J. *et al.* High-Performance Flexible Graphene Field Effect Transistors with Ion Gel Gate Dielectrics. *Nano Letters* **10**, 3464-3466, doi:10.1021/nl101559n (2010).

368 30 Kostarelos, K., Vincent, M., Hebert, C. & Garrido, J. A. Graphene in the Design and Engineering of Next-Generation Neural Interfaces. *Advanced Materials* **29** (2017).

370 31 Benno, M. B. *et al.* Mapping brain activity with flexible graphene micro-transistors. *2D Materials* **4**, 025040 (2017).

372 32 Hébert, C. *et al.* Flexible Graphene Solution-Gated Field-Effect Transistors: Efficient Transducers for Micro-Electrocorticography. *Advanced Functional Materials* **28**, 1703976, doi:doi:10.1002/adfm.201703976 (2018).

375 33 Chen, S., Liu, Y. & Chen, J. Heterogeneous electron transfer at nanoscopic electrodes: importance of electronic structures and electric double layers. *Chemical Society Reviews* **43**, 5372-5386 (2014).

378 34 Brownson, D. A. & Banks, C. E. The electrochemistry of CVD graphene: progress and prospects. *Physical Chemistry Chemical Physics* **14**, 8264-8281 (2012).

380 35 Brownson, D. A. C., Munro, L. J., Kampouris, D. K. & Banks, C. E. Electrochemistry of graphene: not such a beneficial electrode material? *RSC Advances* **1**, 978, doi:10.1039/c1ra00393c (2011).

383 36 Valdes, C. P. *et al.* Speckle contrast optical spectroscopy, a non-invasive, diffuse optical method for measuring microvascular blood flow in tissue. *Biomedical optics express* **5**, 2769-2784 (2014).

386 37 Boas, D. A. & Dunn, A. K. Laser speckle contrast imaging in biomedical optics. *Journal of biomedical optics* **15**, 011109 (2010).

388 38 Shibata, M. & Suzuki, N. Exploring the role of microglia in cortical spreading depression in neurological disease. *Journal of Cerebral Blood Flow & Metabolism* **37**, 1182-1191, doi:10.1177/0271678x17690537 (2017).

391 39 Mitra, A. & Raichle, M. E. How networks communicate: propagation patterns in spontaneous brain activity. *Phil. Trans. R. Soc. B* **371**, 20150546 (2016).

393 40 Herreras, O. Local field potentials: myths and misunderstandings. *Frontiers in neural circuits* **10**, 101 (2016).

395 41 Massimini, M., Huber, R., Ferrarelli, F., Hill, S. & Tononi, G. The sleep slow oscillation as a traveling wave. *Journal of Neuroscience* **24**, 6862-6870 (2004).

397 42 Capone, C. *et al.* Slow Waves in Cortical Slices: How Spontaneous Activity is Shaped by Laminar Structure. *Cerebral Cortex*, 1-17 (2017).

399 43 Carlson, A. P. *et al.* Cortical spreading depression occurs during elective neurosurgical procedures. *Journal of neurosurgery* **126**, 266-273 (2017).

401

Acknowledgments

Author contributions

E.M.C. did most of the fabrication and characterization of the gSGFET arrays, contributed to the design and performance of the *in vivo* experiments, analyzed the data and wrote the manuscript. X.I. designed the neural probes and fabricated the microelectrode arrays. A.B.C. contributed to the fabrication and characterization of the gSGFET arrays. M.D. performed the *in vivo* experiments. P.G., C.H., J.B. and E.P.A. contributed to the growth of the CVD graphene. E.P.A., E.dC. and J.M.dC.S. contributed to the transfer of graphene. E.P.A., E.dC.G. and G.R. contributed to the characterization of CVD graphene. J.M.A. contributed to the fabrication of the custom electronic instrumentation and development of a python-based user interface. A.C. contributed to the propagation analysis. T.Dr., E.V. and T.Du. contributed to the *in vivo* measurements and analysis of cerebral blood flow. M.D., M.S.V., A.G.B, R.V. and J.A.G. participated in the design of the *in vivo* experiments and thoroughly reviewed the manuscript. A.G.B. contributed in the design and fabrication of the custom electronic instrumentation, development of a custom gSGFET python library and in the analysis of the data. All authors read and reviewed the manuscript.

Competing interests

The authors declare no competing interests.

Methods

Graphene growth and characterization

Graphene layers were grown by Chemical Vapor Deposition (CVD) using one of the following procedures: a) A lamp-heated rapid thermal CVD equipment from Jipelec and 25 µm thick, 99.8 % metal basis copper foil provided by AlfaAesar have been employed. Prior to graphene CVD, copper foils were sequentially cleaned in acetic acid and acetone, and finally rinsed in isopropyl alcohol (IPA). Sample dimensions were 6 x 5 cm^2. Growth processing conditions consisted in 10 minutes at 750 °C, 200 sccm H_2 plus 5 minutes at 800 °C, 25 sccm CH_4 / 200 sccm H_2. b) Chemical vapour deposition on a 4.5x7 cm^2 copper foil (Alfa Aesar, annealed, Coated). Prior to the growth, the copper foil was electropolished during 5 min at a fixed current density of 62 mA/cm^{-2} in a solution containing H_2O (1 L) + H_3PO_4 (0.5 L) + ethanol (0.5 L) + isopropanol (0.1 L) and urea (10 g). Then the copper foil was loaded in a planar quartz tube (1600x60 mm) heated by a three zone oven. A first annealing step at 1015 ºC under a 400 sccm argon flow at 100 mbar during 1 h was followed by a 15-

443 min growth step at 12 mbar under a gas mixture of 1000 sccm argon, 200 sccm hydrogen and 2 sccm
444 of methane. The sample was then cooled down under a 400 sccm argon flow by removing the quartz
445 tube from the oven. A complete Raman characterization was performed on each sample using a
446 Witec spectrograph (Fig.S1a-d). Raman maps of 30x30 μm^2 were registered with a spatial resolution
447 lower than 1 μm^2 (using a 50x objective). We used a 488 nm excitation wavelength to minimize the
448 cooper substrate luminescence signal. The laser power was kept below 1.5 mW to avoid sample
449 heating. A 600 g/nm grating was used to provide a pixel to pixel spectral resolution below 3 cm^{-1}.

gSGFET array fabrication and characterization

451 Four-inch silicon wafers were used as a support to build the devices. First, a 10-μm-thick polyimide
452 layer (PI-2611, HD MicroSystems) was spin-coated to be used as substrate and hard-baked at 350ºC
453 to complete the imidation process. Graphene transistors were fabricated in a sandwich-like structure.
454 For that, a first layer of metal (Ti/Au, 10/100 nm) was evaporated and defined in a standard lift-off
455 process using the image reversal photoresist AZ5214E (Clariant GmbH, Germany). Then, single-
456 layer graphene was transferred by electrochemical delamination[1]. After removing the PMMA
457 protection layer, the graphene active areas were defined by means of an oxygen-based reactive ion
458 etching (RIE). A second metal layer (Ni/Au, 20/200nm) was evaporated and defined in a similar
459 standard lift-off process avoiding the use of ultrasounds in order to maintain graphene integrity. SU-8
460 (SU-8 2005, MicroChemCorp., USA) a permanent epoxy-based negative photoresist was used to
461 passivate the metal leads while defining the graphene channel and metal contacts. Finally, the
462 polyimide substrate was structured in a deep-RIE process using the thick AZ9260 positive
463 photoresist (Clariant GmbH, Germany) as an etching mask. Polyimide probes were directly peeled
464 off from the wafer and placed in a zero insertion force (ZIF) connectors to be interfaced with our
465 custom electronic instrumentation. Current-voltage measurements of graphene transistors were
466 performed in common gate mode with a fixed drain-source voltage (V_{DS}=50 mV) varying the gate-
467 source voltage (V_{GS}) vs. a Ag/AgCl reference electrode in 0.01 M PBS solution. Steady-state was
468 ensured by acquiring only after time derivative of 1 s of current is below 5e-7 A/s. The total leakage
469 current was measured for the whole array and corresponds to the sum of the individual leakage
470 currents of all transistors in the array. The frequency response of the transconductance was measured
471 by applying a sum of sinusoidal signals at the electrolyte solution through the reference electrode and
472 by measuring the modulation of the drain current. Measures were split into two bands, low
473 frequencies (≈0-10 Hz) in which drain-source current was simultaneous acquired for all transistors in
474 a probe, and high frequencies (10 Hz-30 kHz) in which each transistor was recorded individually.

Microelectrode array fabrication and characterization

476 The flexible microelectrode array was fabricated in polyimide in a very similar process. Here, a
477 Ti/Au (20/200 nm) metal layer was evaporated on a 10 µm-thick polyimide-covered four-inch silicon
478 wafer to define the metal tracks and the microelectrodes, while a second polyimide layer (2 µm thick)
479 was used as the passivation layer. Two subsequent etching steps were used to open, firstly, the
480 microelectrode active areas and, secondly, to structure the polyimide in order to define the probe
481 geometry which is the same as in Illa et. al.[2]. Platinum black was deposited in some electrodes by
482 constant polarization amperometry. A voltage of -0.2V against a Ag/AgCl reference electrode was
483 applied during 15 s. Impedance spectra were measured against a Ag/AgCl reference electrode using a
484 Solartron SI 1260 equipment (Solarton analytical, UK) with 20 mV signal amplitude.

In vivo recordings

486 Eight adult male Wistar rats (225-375 g) were used in this study. Animals were deeply anaesthetized
487 with isoflurane (4% induction, 1-3% maintenance) and all pressure and incision points were
488 infiltrated with local anesthetic lidocaine. Once under the surgical plane of anesthesia, animals were

489 transferred to a stereotaxic frame with body temperature constantly monitored and maintained at
490 37ºC by means of a thermal blanket. A craniotomy and durotomy were performed on the left
491 hemisphere over either the primary somatosensory (S1, AP: X to Y from bregma) or visual (V1)
492 cortices in order to record with surface or penetrating probes, respectively. Additionally, a
493 craniotomy and durotomy were performed over the prefrontal cortex to topically administer 5 mM
494 KCl to induce cortical spreading depression. A Ag/AgCl electrode was inserted in temporal muscle
495 and used as reference. A custom electronic instrumentation was used which provides the current-to-
496 voltage conversion and the bias control for each channel. The instrumentation splits the recorded
497 signals into two bands with different gains: low-pass filtered (< 0.16 Hz, 10^4 gain) and band-pass
498 filtered (0.16 Hz $<$ f $<$ 160 kHz, 10^6 gain). The low-pass filtered signals and bias control is managed
499 by a data acquisition system (National Instruments USB-6353), while the band-pass filtered signals
500 were directly acquired by a commercial electrophysiological recording system consisting of a
501 programmable gain amplifier (Multichannel Systems, GmbH) and digitizer interface (CED 1401 and
502 Spike2 software, Cambrigde Electronic Design, UK). LPF band was sampled at 1 Hz and BPF at 5
503 kHz. Prior to the beginning of the recordings, the transfer curve of the gSGFET was measured *in situ*
504 to determine the best bias point, generally around -0.1 V of the CNP. For the electrode and transistor
505 comparison experiment, a custom Simulink model was used to simultaneously measure graphene
506 transistors through an adapted g.HIamp biosignal amplifier(g.tec medical engineering GmbH,
507 Austria) while microelectrodes were recorded using an g.USBamp (g.tec medical engineering GmbH,
508 Austria). The same Ag/AgCl reference electrode was used by both amplifiers and signals were
509 sampled at 5 kHz.

Laser speckle contrast imaging

511 For the measurement of the regional cerebral blood flow (rCBF), a laser speckle contrast imaging
512 (LSCI) system was used which consists of a continuous-wave temperature-controlled laser diode
513 (785 nm, Thorlabs, Germany) for homogenous full-field illumination and a charge-coupled device
514 camera (sc640-120fm, Basler, Germany), with an exposure time of 5 ms, which captures the diffused
515 light scattered from the imaging area. The speckle contrast was calculated for the predefined region
516 of interest (ROI) at each pixel in temporal domain over 100 frames, to ensure good signal-to-noise
517 ratio. The statistics of different noise sources[3] was accounted for when calculating the speckle
518 contrast. Speckle contrast was then related to a rCBF index (BF) as reported in [4,5]. Finally, the
519 relative blood flow (ΔrCBF) was calculated as:

520
$$\Delta rCBF = \frac{BF - BF_B}{BF_B} * 100 \ [\%]$$

521 where BF_B corresponds to the basal regional blood flow.

Data Analysis

523 All data were analyzed using Python 2.7 packages (Matplotlib, Numpy and Neo) and the custom
524 library PyGFET (https://github.com/aguimera/PyGFET). The conversion of the recorded current
525 signals (LPF and BPF) to a voltage signal was performed by summation and interpolation in the *in*
526 *vivo* measured transfer curve of the corresponding gSGFET at the bias point. For visualization
527 purposes microelectrode recordings were filtered (band-stop, 48-52 Hz) and down sampled at 300Hz.
528 For the propagation analysis, the baseline of the signal was estimated as the mean value of the signal
529 until the positive deflection. We defined the onset of the CSD as the onset of the negative shift and
530 detected it using a threshold (Fig. S7a). We defined the WaveTime of each wave as the mean time of
531 the triggers detected in the 16 transistors and constructed a TimeLagMatrix containing time lags for
532 each channel computed with respect to the WaveTime (Fig. S7c). We interpolated the known time

lags with a thin-plate smoothing spline technique. The velocity of the propagation has been estimated computing the gradient of the TimeLagMatrix on the grid[6]. To determine the direction of the waves, a vector starting at the point with higher negative delay (leader of the propagation) and pointing to the one with the highest positive delay (follower of the propagation) was transformed into polar coordinates to obtain the angle (Fig. S7b).

Methods References

1   de la Rosa, C. J. L. *et al.* Frame assisted H[sub 2]O electrolysis induced H[sub 2] bubbling transfer of large area graphene grown by chemical vapor deposition on Cu. *Applied Physics Letters* **102**, 022101-022104 (2013).

2   Illa, X., Rebollo, B., Gabriel, G., Sánchez-Vives, M. V. & Villa, R. in *SPIE Microtechnologies.* 951803-951803-951806 (International Society for Optics and Photonics).

3   Valdes, C. P. *et al.* Speckle contrast optical spectroscopy, a non-invasive, diffuse optical method for measuring microvascular blood flow in tissue. *Biomedical optics express* **5**, 2769-2784 (2014).

4   Boas, D. A. & Dunn, A. K. Laser speckle contrast imaging in biomedical optics. *Journal of biomedical optics* **15**, 011109 (2010).

5   Bandyopadhyay, R., Gittings, A., Suh, S., Dixon, P. & Durian, D. J. Speckle-visibility spectroscopy: A tool to study time-varying dynamics. *Review of scientific instruments* **76**, 093110 (2005).

6   Capone, C. *et al.* Slow Waves in Cortical Slices: How Spontaneous Activity is Shaped by Laminar Structure. *Cerebral Cortex*, 1-17 (2017).